Phase transitions and molecular dynamics of *n*-hexadecanol confined in silicon nanochannels

R. Berwanger,[1] A. Henschel,[2] K. Knorr,[2] P. Huber,[2] and R. Pelster[1]
[1]*Universität des Saarlandes, FR 7.2 Experimentalphysik, 66041 Saarbrücken, Germany*
[2]*Universität des Saarlandes, FR 7.3 Technische Physik, 66041 Saarbrücken, Germany*
(Received 29 December 2008; revised manuscript received 12 February 2009; published 31 March 2009)

We present a combined x-ray diffraction and infrared spectroscopy study on the phase behavior and molecular dynamics of *n*-hexadecanol in its bulk state and confined in an array of aligned nanochannels of 8 nm diameter in mesoporous silicon. Under confinement, the transition temperatures between the liquid, the rotator R_{II}, and the crystalline C phase are lowered by approximately 20 K. While bulk *n*-hexadecanol exhibits at low temperatures a polycrystalline mixture of orthorhombic β and monoclinic γ forms, geometrical confinement favors the more simple β form: only crystallites are formed, where the chain axis is parallel to the layer normal. However, the γ form, in which the chain axis is tilted with respect to the layer normal, is entirely suppressed. The β crystallites form bilayers that are not randomly orientated in the pores. The molecules are arranged with their long axis perpendicular to the long channel axis. With regard to the molecular dynamics, we were able to show that confinement does not affect the innermolecular dynamics of the CH_2 scissor vibration and to evaluate the intermolecular force constants in the C phase.

DOI: 10.1103/PhysRevB.79.125442 PACS number(s): 64.70.Nd, 61.46.Hk, 81.07.−b, 61.43.Gt

I. INTRODUCTION

The physical properties of condensed matter spatially confined in pores or channels of a few nanometers in diameter can differ markedly from the behavior in the bulk state. In particular, phase transitions can be entirely suppressed or significantly altered in comparison to their bulk counterparts.[1–4] Also the dynamics of condensed matter confined in mesopores, most prominently in the vicinity of glass transitions,[5–14] can be affected markedly.

Intimately related to these changes in the phase-transition phenomenology, the architectural principles of molecular solids can substantially differ in the spatially confined state from the bulk state. This depends, however, sensitively on the complexity of the building blocks. For simple van der Waals systems, such as Ar and N_2, a remarkable robustness of the bulk structures has been found for the solid state under confinement.[15–17] By contrast, the structural properties of pore fillings built out of more complex building blocks, such as linear hydrocarbons[18–22] or liquid crystals,[23,24] are very susceptible to confinement on the mesoscale and nanoscale. For example, a quenching of the lamellar ordering of molecular crystals of *n*-alkanes has been observed in tortuous silica mesopores of Vycor.[25] However, in tubular channels of mesoporous silicon, this building principle of hydrocarbon molecular crystals survives, albeit a peculiar texture has been observed for the pore-confined solids.[19] The long axes of the molecules and thus the stacking direction of the lamellae are oriented perpendicular to the long axis of the pores.

Here we present an experimental study on a medium-length linear alcohol $C_{16}H_{33}OH$, a representative of the 1-alcohol series, imbibed in mesoporous silicon. We explore the phase behavior of the confined alcohol by a combination of x-ray diffraction and infrared (IR) spectroscopy measurements. As we shall demonstrate, we profit in those experiments both from the parallel alignment of the silicon channels and from the transparency of the silicon host in the infrared region.

II. EXPERIMENTAL

The porous silicon samples used in this study were prepared by electrochemical etching of a heavily *p*-doped (100) silicon wafer (producer: SiMat, Landsberg, Germany; specific conductivity: $\rho=0.01-0.025\ \Omega$ cm) with a current density of $13\frac{\mathrm{mA}}{\mathrm{cm}^2}$ in a solution composed of HF, ethanol, and H_2O (1:3:1 per volume).[26–28] These conditions led to a parallel arrangement of noninterconnected channels oriented with their long axes along the ⟨100⟩ crystallographic direction of silicon, which coincides with the normal of the wafer surface. After the porous layer had reached the desired thickness of 70 microns, the anodization current was increased by a factor of 10 with the result that the porous layer was released from the bulk wafer underneath. Using nitrogen sorption isotherms at $T=77$ K, we determined a porosity of 60% and a mean channel diameter of 8 nm. The single crystalline character of the matrix was checked by x-ray diffraction. Transmission electron micrographs of channel cross sections indicate polygonal, rough channel perimeters rather than circular, smooth circumferences.[29]

The matrix both for the infrared spectroscopy and the x-ray measurements was filled completely via capillary action (spontaneous imbibition) with liquefied $C_{16}H_{33}OH$.[30] Bulk excess material at the surface was removed by paper tissues.

Infrared spectra in a range of wave numbers $\bar{\nu}$ from 4000 to 800 cm^{-1} with a resolution of 1 cm^{-1} were measured with a Fourier transform spectrometer [Fourier transform infrared (FTIR) Perkin Elmer System 2000]. This range corresponds to frequencies from 3×10^{13} Hz to 1.2×10^{14} Hz (wavelengths from 10 to 2.5 μm). For both the bulk material and the filled porous samples, the same sample holder was used, i.e., a copper cell with two transparent KBr windows. In the confinement experiments, the long channel axes were oriented parallel to the beam axis, i.e., perpendicular to the electric field vector. The sample holder was placed into a cryostat (a closed cycle refrigerator CTI cryogenics, model

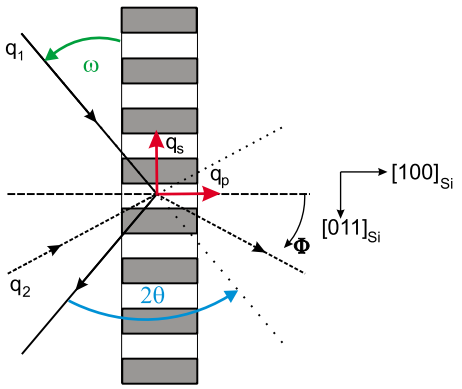

FIG. 1. (Color online) The angular variable Φ ($\Phi=\omega-\theta$ with $\Phi=0°$ for scans along q_p and $\Phi=90°$ for scans along q_s) is indicated. Also shown are the incoming and outgoing x-ray beams for scans along q_p (solid lines: wave vector component parallel to the pore axis, this means reflection geometry), and along q_s (dashed lines: wave vector component perpendicular to the pore axis; this is transmission geometry). For scans along q_p, the detector angle 2θ and the rotation angle ω are represented.

22) allowing us to vary the temperature from 50 to 340 K. The temperature was controlled with a LakeShore 340 temperature controller with a precision of ± 0.25 K. All IR spectra that we show in the following were measured during cooling (typical cooling rates were on the order of 0.5 K/min). Heating scans show the same behavior except for the transition temperatures, which are some degrees higher (see below).

For the x-ray measurements, the sample was mounted on a frame in a sample cell consisting of a Peltier-cooled base plate and a Be cap. The cell was filled with He gas for better thermal contact. The Be cap sits in a vacuum chamber, the outer jacket of which has Mylar windows allowing the passage of the x-rays over a wide range of scattering angles θ within the scattering plane (see Fig. 1). But the setup allowed practically no tilt with respect to the scattering plane. The temperature was controlled by a LakeShore 330 over an accessible range from 245 up to 370 K. The measurements were carried out on a two-circle x-ray diffractometer with graphite-monochromatized Cu K_α radiation emanating from a rotating anode. The porous sheet was mounted perpendicular to the scattering plane. The two angles that could be varied were the detector angle 2θ and the rotation angle ω about the normal of the scattering plane. The samples were studied as a function of temperature by performing several Φ scans. In this paper, we concentrate on radial 2θ-ω scans in reflection geometry, i.e., along q_p with $\Phi=0°$, and in transmission geometry, i.e., along q_s with $\Phi=90°$ (see Fig. 1).

A. Structure of bulk *n*-hexadecanol

n-hexadecanol, $C_{16}H_{33}OH$, is an almost rodlike molecule with a length of 22 Å and a width of 4 Å. The C atoms of the backbone are in an all trans configuration so that they are located in a plane.[25]

At low temperatures, *n*-alcohols form bilayered crystals in two possible modifications: the so-called γ form, i.e., a

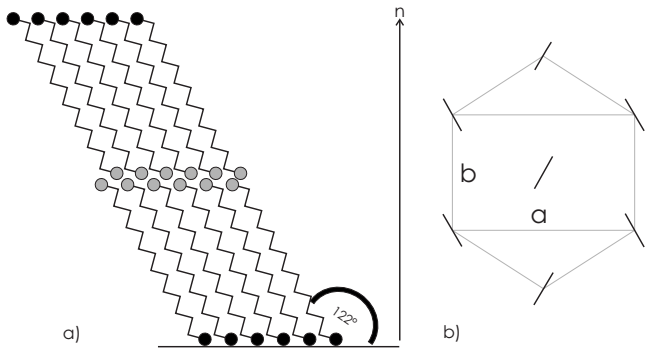

FIG. 2. γ form of the crystalline low-temperature phase of bulk $C_{16}H_{33}OH$ ($T \leq 310$ K). The structure is monoclinic. The left sketch shows the orientation of the molecules with respect to the layer normal n, the right sketch the in-plane arrangement, i. e., a projection of the backbones into the a-b plane. Compare with the β form sketched in Fig. 3.

monoclinic structure as sketched in Fig. 2 [C_{2h}^6-A2/a (Refs. 31 and 32)], or the so-called β form, i.e., an orthorhombic structure as sketched in Fig. 3.[33] In the γ form, the molecules include an angle of 122° with the layer plane. Within the layers, they are close packed in a quasihexagonal two-dimensional (2D) array described by the rectangular in-plane lattice parameters a and b (according to Ref. 32 $a=7.42$ Å and $b=4.93$ Å holds, so that $a/b=1.5$). There are two different alternating orientations for the C-C plane of the backbone leading to a herringbone structure [see Fig. 2(b)]. The β form exhibits an identical orientational order of the backbone, but the molecules' axes remain perpendicular to the layers as sketched in Fig. 3.[33] In addition, gauche and trans conformations of the CO-bond alternate with molecules in this phase, while they are in an all trans configuration in the γ form. In general, the γ form dominates at low temperatures for the even alcohols, while the β form is more frequent in odd *n*-alcohols.[33,34] For *n*-hexadecanol, both the orthorhombic β form[33] and the monoclinic γ form[31,32] are reported.

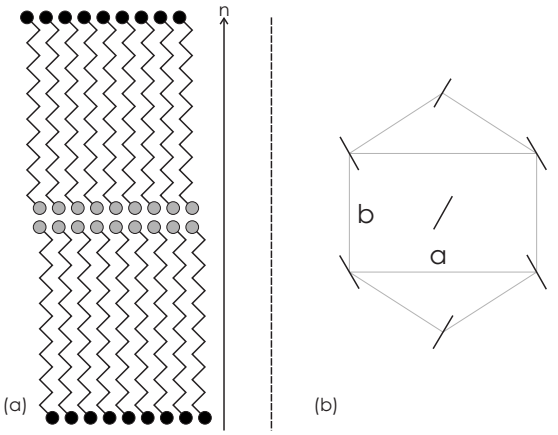

FIG. 3. β form of the crystalline low-temperature phase of $C_{16}H_{33}OH$. In contrast to the γ form [see Fig. 2(a)], the long chain axes are not tilted but parallel to the layer normal n, i. e., the structure is orthorhombic. Bulk $C_{16}H_{33}OH$ can exhibit a polycrystalline mixture of γ and β forms (see Sec. II A). Confinement into nanopores leads to the β form (see below, Sec. III A).

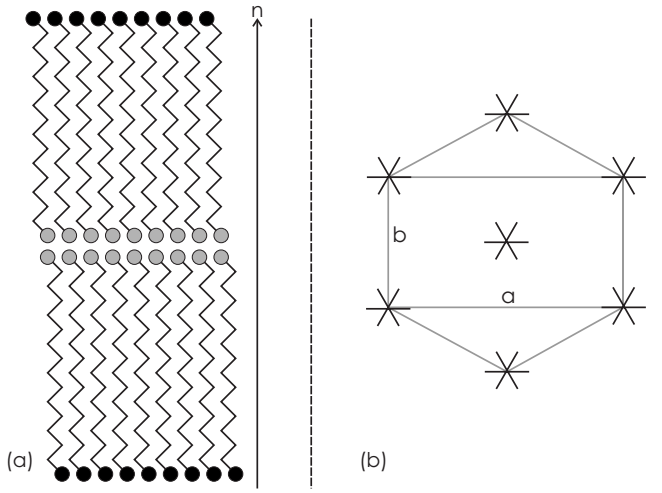

FIG. 4. Structure of bulk n hexadecanol in the rotator-(II) phase (for $310 \leq T \leq 322$ K), a hexagonal arrangement. The right picture shows the perfect hexagonal lattice in the a-b plane. Confined $C_{16}H_{33}OH$ exhibits the same structure in its rotator phase, but in a different temperature range (see Table II).

Depending on the preparation conditions, it is possible to obtain a polycristalline mixture of the monoclinic γ and the orthorhombic β forms.[34]

Upon heating, the crystalline phase undergoes a transition into a so-called rotator-(II) phase R_{II}, which is schematically depicted in Fig. 4. (For several alkanes, there also exists a rotator-(I) phase R_I, where the molecules switch between two equal positions.). This phase has a hexagonal in-plane arrangement with the c direction perpendicular to the cell base. The hexagonal arrangement can be indexed with an orthorhombic cell with a ratio of rectangular basal lattice parameters of $a/b=\sqrt{3}$.[35] On a microscopic level, the change in the center of mass lattice from the low-temperature crystalline phase to the rotator phase can be attributed to the onset of hindered rotations of the molecules about their long axes between six equivalent positions [the stars in Fig. 4(b)]. Further heating above 322 K leads to the liquid state.[35]

III. RESULTS

A. Structure of confined *n*-hexadecanol

We have determined structures, phase sequences, and transition temperatures of $C_{16}H_{33}OH$ confined in mesoporous silicon by x-ray diffractometry. The upper panel in Fig. 5 shows diffraction patterns along q_p at selected temperatures while cooling. The appearance of a broad Bragg peak at $2\theta \simeq 21°$ indicates solidifaction. Its position is compatible with the leading hexagonal in-plane reflection of the R_{II} phase. Upon further cooling, a second peak at $2\theta \simeq 24°$ shows up. This change in the diffraction pattern indicates an uniaxial deformation of the hexagonal lattice. Both reflections can be mapped on a 2D rectangular mesh characteristic of an uniaxially deformed hexagonal cell. The overall resulting pattern is, however, incompatible with the monoclinic structure of the low temperature bulk crystalline phase.

Additionally to the q_p scans, we performed also scans for a variety of additional orientations of the scattering vector

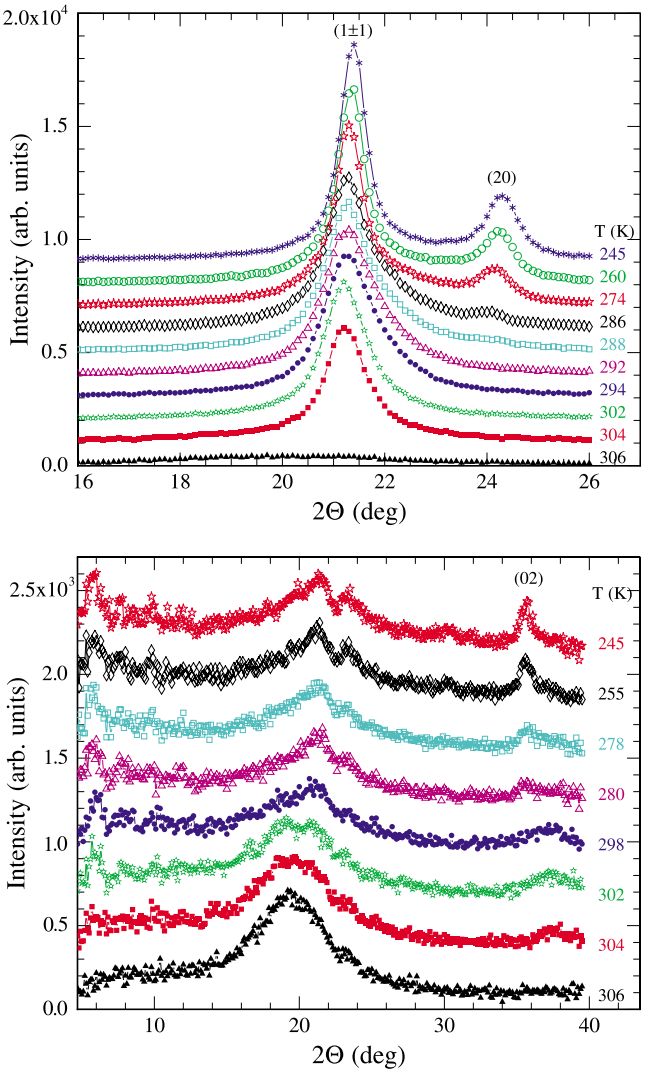

FIG. 5. (Color online) Upper panel: diffraction pattern of q_p scans of pore confined $C_{16}H_{33}OH$ while cooling at selected temperatures. Lower panel: diffraction pattern of q_s scans at selected temperatures while cooling. The leading in-plane reflections are barely visible. Moreover, at lower angles ($2\theta \leq 10$), there are very weak and diffuse layering reflections.

with regard to the long axis of the channels. These patterns differ markedly, which is indicative of a strong texture of the pore-confined cystallized alcohol. It is not powder in the crystallographic sense. In particular, there are strong in-plane reflections and no layering reflections for scans along q_p, while the q_s scans for the same sample show at least very weak reflections characteristic of a bilayer stacking and only very weak leading in-plane reflections (see Fig. 5). An analysis of the width of the layering reflections yields a coherence length of $7(\pm 1.5)$ nm.

As discussed in more detail in Refs. 19 and 36, the overall picture which emerges from these results can be summed up as follows. The alcohol molecules form orthorhombic structures with a bilayer-stacking direction along the c direction. Within the bilayers (the a-b plane), the molecules' backbones are untilted with regard to the stacking direction and the backbones are orientationally either fully ordered (in a her-

TABLE I. Lattice parameters a and b of bulk and confined $C_{16}H_{33}OH$ and the diagonal $d=\sqrt{a^2+b^2}$ of the subcell (see Fig. 14). The confined data result from our x-ray measurements and the bulk data are taken from the literature (Ref. 32).

	Bulk	Confinement	
	Cryst.	R_{II}	Cryst.
a (Å)	7.42	8.35	7.33
b (Å)	4.93	4.82	5.04
a/b	1.51	$\sqrt{3}$	1.45
d (Å)	8.91	9.64	8.90

ringbone fashion) or partially ordered, as known from the R_I phase of n-alkanes. The superlattice reflection characteristic of the full herringbone-type orientational ordering has been searched for and could weakly be detected at low temperatures. The degree of uniaxial deformation of the hexagonal center of mass cell quantified by the deviation of the ratio a/b from its value in the hexagonal phase ($\sqrt{3}$) also indicates a full orientational-ordered state (see Table I).[32] Thus, the diffraction data are compatible with the bulk β modification discussed above. This conclusion is also supported by an analysis of the infrared spectroscopy data sets presented below.

More importantly, the peculiar dependency of the diffraction patterns on the orientation of the q vector with regard to the silicon host indicates that the bilayer stacking direction is perpendicular to the long axis of the channels and, consequently, that the long axis of the molecules is oriented perpendicular to the long axis of the channels (see Fig. 6). At first glance, this finding may appear somewhat counterintuitive. Albeit it can be understood as resulting from the crystallization process in a strongly anistropic capillarylike-confined liquid.[19,37] It is a well-established principle in single crystal growth that in narrow capillaries, the fastest growing crystallization direction prevails over other directions and propagates along the long axes of capillaries.[38] For layered molecular crystals of rodlike building blocks, this direction is an in-plane direction, which is perpendicular to the long axis of the rods. If this direction is aligned parallel to the silicon nanochannels due to the crystallization process, it dictates a perpendicular arrangement of the molecules' long axes with regard to the long channel axis, in agreement with the diffraction results presented here.

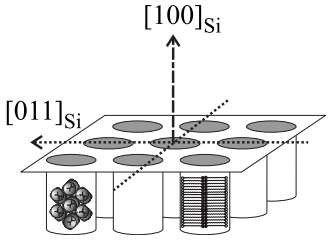

FIG. 6. Sketch of the orientation of pore-condensed $C_{16}H_{33}OH$ in the porous sheet. Left pore: view on the rectangular in-plane arrangement of the molecules. Right pore: bilayered crystal; the long molecule axis is oriented perpendicular to the pore axes. At maximum, two bilayers fit into a pore.

TABLE II. Transition temperatures as determined by x-ray experiments of confined and bulk $C_{16}H_{33}OH$ (Ref. 35). They agree with those inferred from IR measurements (CH_2-scissoring vibration) (see Figs. 10 and 11).

	Fluid R_{II}	R_{II}-C	Fluid-R_{II}	R_{II}-C
confined (cooling)	304	291		
confined (heating)	312	293		
bulk			322	310

The temperature-dependent diffraction study allows us to gain additional information on the relative stability of the different nanochannel-confined phases. In Table II, we display the phase-transition temperatures of confined $C_{16}H_{33}OH$ as inferred from the appearance or disappearance of characteristic Bragg peaks. There is a hysteresis between heating and cooling for both the fluid-R_{II}- and the R_{II}-C transition (8 K and 3 K, respectively). Compared to the bulk data (see also Table II), the transition temperatures of pore confined $C_{16}H_{33}OH$ are lowered. On cooling, the lowering is on the order of $\Delta T=18$ K for the fluid-R_{II} transition and $\Delta T=26$ K for the R_{II}-C transition. This observation is analogous to phase-transitions shifts reported for other pore condensates.[2,3]

Furthermore, the temperature range of the confined R_{II} phase, 14 K upon cooling and 19 K upon heating, is larger than that of the bulk material (12 K). Obviously, confinement stabilizes the orientational-disordered R_{II} phase, similarly as has been found for n-alkanes[19] and for other orientational disordered plastic phases under spatial confinement.[4]

Since the pores were completely filled at higher temperatures, when hexadecanol is in its liquid state, the pore filling at low temperatures does not consist only of bilayer crystals: the change of volume at the R_{II}-C phase transition is about 10% (see Fig. 7), so that there are voids and/or molecules that are not part of a bilayer crystal. However, our experiments do not give us information about their spatial arrangement.

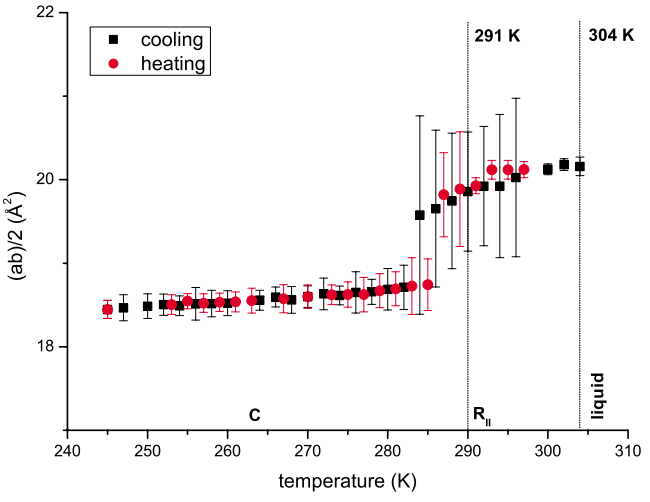

FIG. 7. (Color online) Temperature dependence of the area per molecule A for $C_{16}H_{33}OH$ confined in porous silicon.

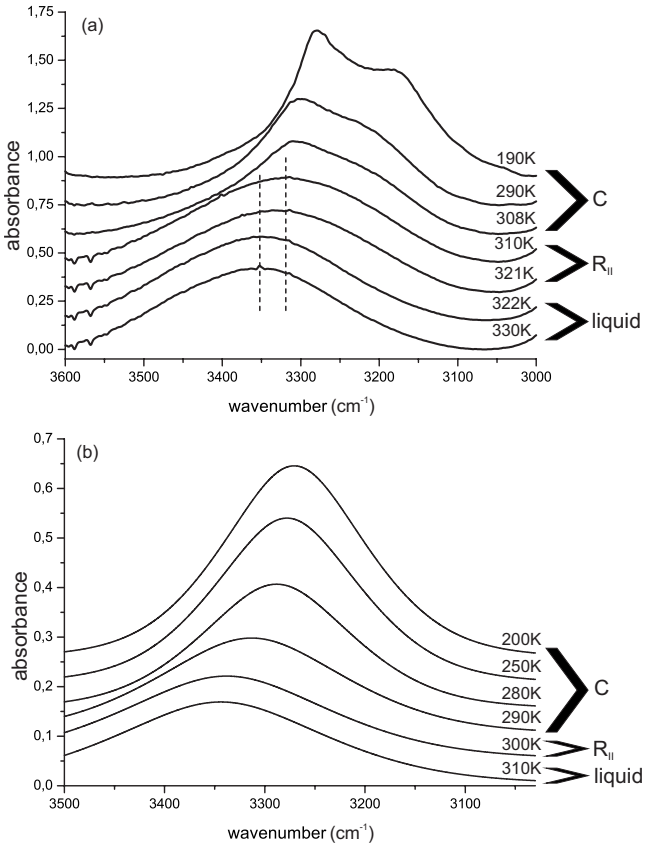

FIG. 8. (a) IR spectrum in the OH-stretching range for bulk $C_{16}H_{33}OH$. At lower temperatures, the peak shifts to lower wave numbers and then splits into two peaks. (b) Spectrum for confined $C_{16}H_{33}OH$, where no splitting is visible.

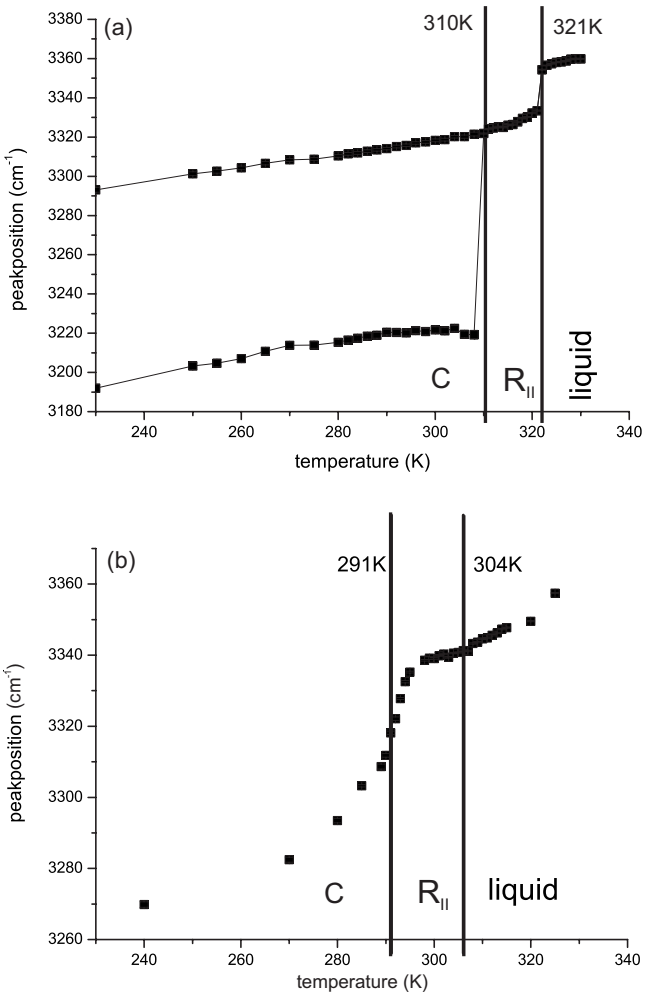

FIG. 9. (a) Wave number $\omega/2\pi c$ of the OH-stretching peak vs temperature for bulk $C_{16}H_{33}OH$ [compare with Fig. 8(a)]. Three different phases are visible: (a) above 321 K, (b) from 310 to 321 K, where the peak position appears at lower wave numbers, and (c) below 310 K where the peak splits up into two peaks. (b) Wave number of the OH-stretching peak for confined $C_{16}H_{33}OH$ [compare with Fig. 8(b)]. The transition between the C and the R_{II} phase seems to be smeared in a range around $T=291\pm5$ K. The R_{II}-liquid transition does not affect the OH stretching.

B. Molecular dynamics

The dynamics of bulk $C_{16}H_{33}OH$ has already been investigated in IR measurements in the past.[31,33] In order to show later on how the molecular dynamics is affected by spatial confinement on the nanometer scale, we display some of our bulk spectra in the following. Here we focus on two characteristic vibrations, the OH-stretching and the CH_2-scissoring vibrations.

Figures 8(a) and 9(a) show the bulk spectra of the OH-stretching band in the respective phases (compare with Figs. 2–4). In the liquid state (above 322 K), the peak maximum is located at about 3345 cm^{-1}. A decrease in temperature below 321 K yields a shift of the peak position to about 3325 cm^{-1} indicating the molecular rearrangement in the R_{II} phase. A further decrease in temperature below 310 K results in a splitting into two peaks at approximately 3310 cm^{-1} and 3220 cm^{-1}. Confined $C_{16}H_{33}OH$ shows a different behavior. There is only one peak in the whole temperature range, the position of which changes reflecting the transition between liquid phase and R_{II} phase as well as between R_{II} phase and C phase [see Figs. 8(b) and 9(b)].

The fact that the OH band of bulk $C_{16}H_{33}OH$ splits at low temperatures while no splitting is observed under confinement confirms the structural differences already observed in the x-ray experiment. For example, Tasumi *et al.*[33] studied bulk alcohols $C_nH_{2n+1}OH$ from $n=11-37$ using infrared spectroscopy; Ventòla *et al.*[34] studied alcohols with $n=17-20$. Those alcohols showing at low temperatures (C phase) the monoclinic γ form, such as $C_{16}H_{33}OH$, exhibit the splitting of the OH-band, while those that take the orthorhombic β form show a single peak. This is due to differences in the spatial arrangement of the hydrogen bonds as well as in the distances of neighboring O-atoms: in the crystalline γ form, where the molecule axes are tilted (see Fig. 2), the molecules show an all trans conformation, and the intralayer O distance ($\simeq$2.74 Å) differs from the interlayer O distance ($\simeq$2.69 Å). However, in the orthorhombic β form (Fig. 3) trans molecules and gauche molecules alternate and the intralayer O distance (2.73 Å) nearly equals the interlayer O distance (2.72 Å), so that the splitting is suppressed.[33] Therefore, the observed OH-band splitting for bulk $C_{16}H_{33}OH$ shows the presence of the γ form. Either the

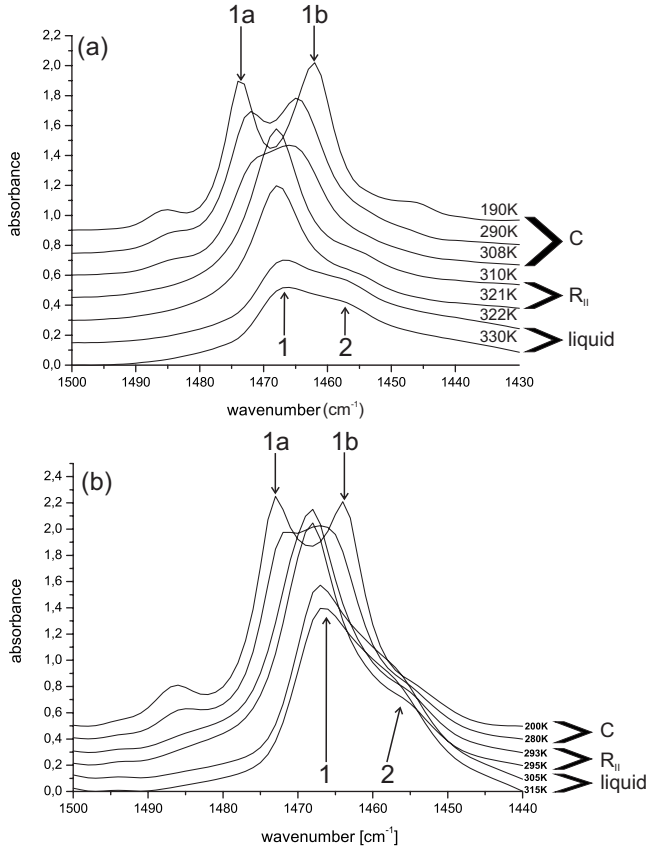

FIG. 10. (a) IR spectrum showing the CH_2 scissor vibration for bulk $C_{16}H_{33}OH$ at various temperatures. (b) IR spectrum showing the CH_2 scissor vibration of $C_{16}H_{33}OH$ confined in mesoporous Si at various temperatures.

whole bulk material exhibits the γ form or there is a mixture of γ and β crystallites. The latter case is frequently observed.[33,34] In fact, in the range of wave numbers from 1150 cm^{-1} to 950 cm^{-1}, where C-C stretching vibrations are visible, we see indications for a superposition of both forms (not shown). On the other hand, pore-confined $C_{16}H_{33}OH$ shows no OH-band splitting at low temperatures. This reflects that the molecular arrangement does not transform in the monoclinic γ form but remains in an orthorhombic structure, i.e., only the β form is present (compare Figs. 2 and 3). This result is in agreement with the x-ray data presented above. Upon cooling, both the bulk and the confined hexadecanol pass from an hexagonal R_{II} phase into a crystalline phase. The bulk material undergoes a stronger structural change, i.e., there is a mixture of the orthorhombic β and the monoclinic γ form. The latter one is suppressed under confinement, so that only the β form remains, which is quite similar to the hexagonal structure of the R_{II} phase. The fact that the crystallites have to fit into nanopores of irregular shape might favor the geometrically more simple β form[3,39] (see Fig. 6).

Now let us turn toward the scissor vibration of the CH_2 groups (bending mode) that will give us information about innermolecular and intermolecular force constants. The spectra are shown in Fig. 10. At first, we want to discuss the bulk material. At high temperatures (liquid state), a superposition

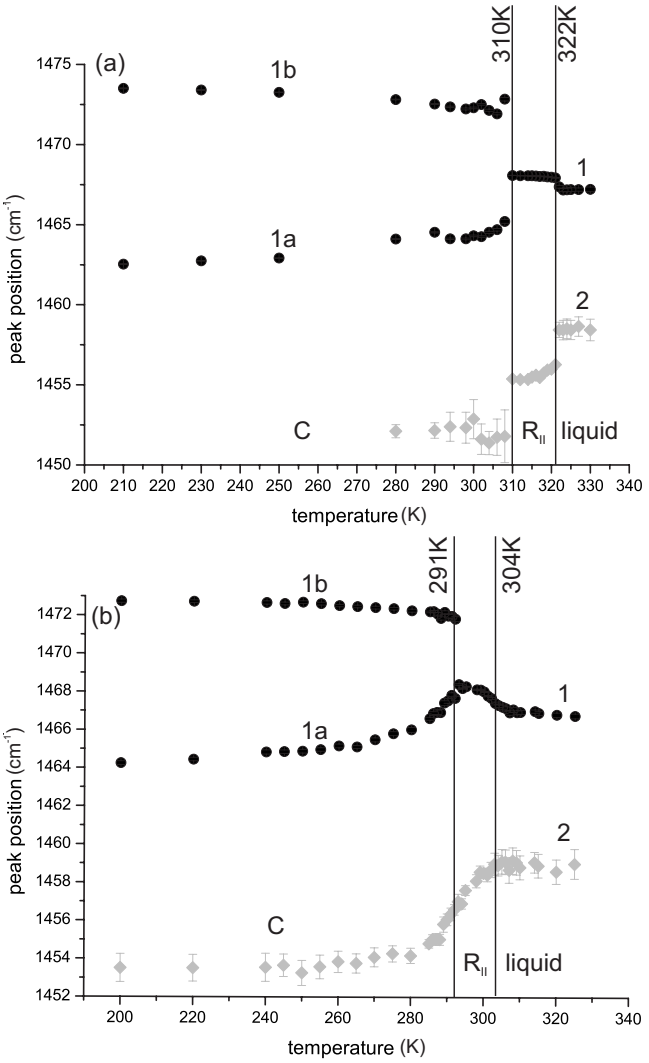

FIG. 11. Wave number of the CH-scissor peak vs temperature for (a) bulk $C_{16}H_{33}OH$ and (b) confined $C_{16}H_{33}OH$ (the peak labels refer to Fig. 10).

of two peaks at 1467 cm^{-1} and 1460 cm^{-1} is observed. In the intermediate temperature range (R_{II} phase; see Fig. 4) the intensity of the peak labeled "1" increases strongly. At low temperatures, (C phase; see Fig. 2) this band splits up into two peaks. The latter transition can be clearly seen in Figs. 11(a) and 12(a), where we display the peak positions and intensities as a function of temperature. The results are similar to those obtained for the bulk state of *n*-paraffines that apart from the missing OH group are similar in their structure, i.e., that have the same CH_2 backbone.[40] In IR spectra, only one CH_2-scissoring band is observed at high temperatures, i.e., intramolecular interactions of the CH_2 groups are too small to lead to a series of distinct peaks. The band splitting at low temperatures has been attributed to intermolecular interactions (see Ref. 40 and text below).

Qualitatively, a behavior similar to that of the bulk state is observed for confined $C_{16}H_{33}OH$ [see Fig. 10(b)]. In the high-temperature liquid phase, two overlapping peaks are visible. The stronger one, i.e., that at higher wave numbers, undergoes an increase in intensity at about 304 K [see Fig.

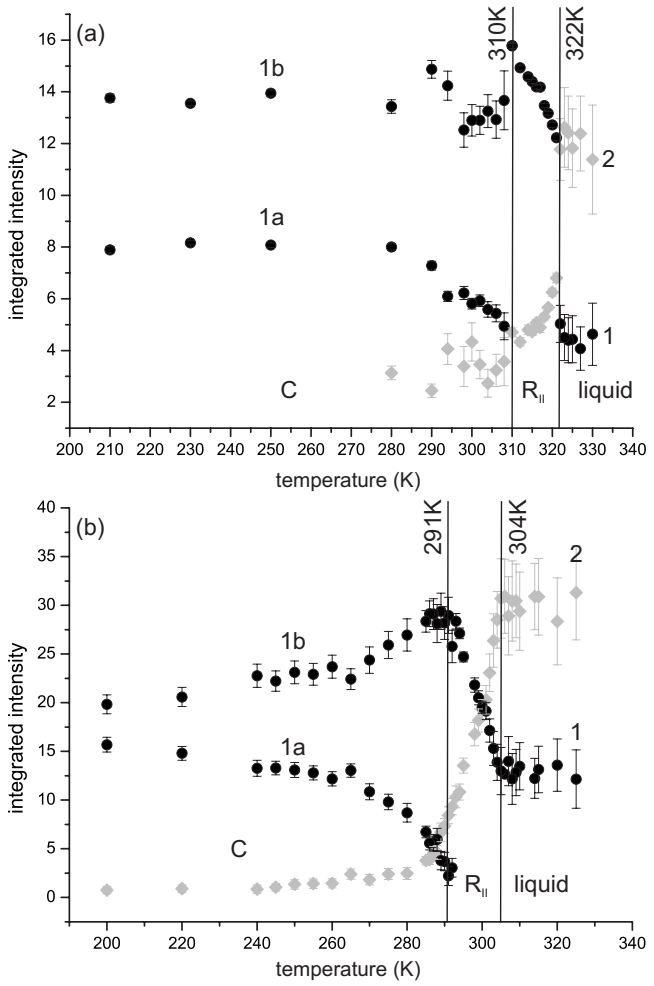

FIG. 12. Integrated intensity of the CH-scissor peak vs temperature for (a) bulk $C_{16}H_{33}OH$ and (b) confined $C_{16}H_{33}OH$ (the peak labels refer to Fig. 10).

12(b)], indicating the transition from the liquid phase to the R_{II} phase, while the secondary peak at lower wave numbers gets weaker and finally disappears. At the second transition temperature of $T=291$ K, the remaining strong peak splits [see also Fig. 11(b)]. The separation is not as distinct as for bulk material. These transition temperatures $T=304$ K and $T=291$ K [see Figs. 11(b) and 12(b)] agree well with those obtained via x-ray measurements (compare with Table II).

In the following, we want to analyze the dynamics of the CH_2 groups in order to check whether it is affected by the geometric confinement, e.g., by an interaction with the pore surfaces, by the limited number of neighboring molecules (finite-size effects), or by structural changes. In a first approximation, we can assume that it is not affected by the stretching of the OH groups. On one hand, there is the scissor vibration, where the angle α between the two CH bonds oscillates around its equilibrium value $\alpha=109.47°$ (see Fig. 13). In addition, symmetric and asymmetric stretching vibrations of the CH bonds are observable (for the values, see Table III). Let f_α and f_d denote the respective force constants. These can be calculated from the measured vibration frequencies using Eqs. (A26)–(A28) [see Appendix A; the difference in calculating f_α via Eq. (A27) or Eq. (A28) is

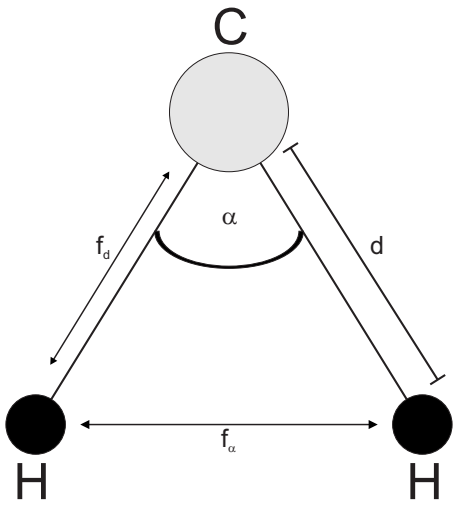

FIG. 13. CH_2 molecules with C-H bond length d, H-C-H angle α, and the resulting inner force constants f_d and f_α.

below 3.5% confirming that the innermolecular coupling terms can be neglected). Table III shows the results for the liquid and the R_{II} phase. Neither the phase transition liquid $\rightarrow R_{II}$ nor the geometrical confinement does markely affect the innermolecular constants.

In the R_{II} phase, the molecules rotate about their long axis, so that the primitive cell consists of only one molecule per layer (see Fig. 4). Therefore, no splitting is observed. But in the C phase (below 310 K for bulk and below 291 K for confined $C_{16}H_{33}OH$), where the molecules are arranged in a herringbone structure, there are two molecules per layer in the primitive cell. So the symmetry of the arrangement allows a splitting of the scissoring band and obviously the molecular interactions are sufficiently strong that we are able to observe a double peak (see above; Figs. 10 and 11). The strength of interaction depends on the distances between neighboring H atoms of adjacent chains and can be analyzed using a formalism developed by Snyder (see Ref. 40 and Appendix B). In Fig. 14 we have sketched the orthorhombic lattice of the crystalline $C_{16}H_{33}OH$ subcell (a view on the

TABLE III. Wave numbers $\bar{\nu}=\omega/(2\pi c)$ (with ω being the angular frequency and c the speed of light) and resulting stretching and bending force constants in the liquid and R_{II} phase of bulk and confined $C_{16}H_{33}OH$. f_α has been evaluated using both Eqs. (A27) and (A28). The difference yields the specified uncertainty. f_α are in units of N/m [see Eq. (A5) in Appendix A and Ref. 41]. To get f_α in units Nm/rad^2, one has to multiply f_α with d^2, where $d=1.09\times10^{-10}$ m is the CH bond length.

	Bulk		Confinement	
	Liquid	R_{II}	Liquid	R_{II}
scissor (cm^{-1})	1467	1467	1467	1467
sym. stretch (cm^{-1})	2854	2851	2854	2851
assym. stretch (cm^{-1})	2927	2921	2924	2918
f_d(N/m)	455	453	454	452
f_α(N/m)	56 ± 1	56 ± 1	57 ± 1	57 ± 1

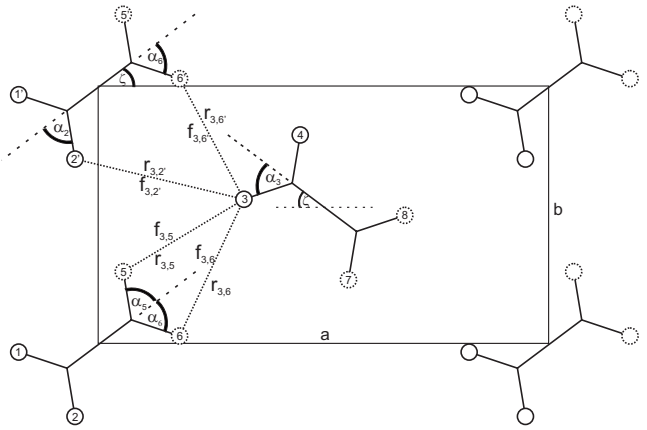

FIG. 14. Lattice of $C_{16}H_{33}OH$ in the C phase of the β form, i.e., a view on the *a*-*b* plane perpendicular to the molecules axis (compare with Fig. 3). Solid circles are H atoms in the same plane; dashed circles are H atoms lying in a plane above.

a-*b* plane perpendicular to the molecules axis). In what follows, we restrict ourselves to this β form that is characteristic for confined $C_{16}H_{33}OH$ (a quantitative analysis of bulk $C_{16}H_{33}OH$ is difficult due to the superposition of β and γ forms). Assuming that the inner force constant f_α does not change at the phase transition, the intermolecular force constants $f_{3,j}$ can be evaluated from the observed splitting of the scissor band as described in Appendix B [see Eq. (B31)]. The values needed are the lattice parameters (see Table I) and the herringbone angle ζ between the projection of the backbone and the *a* axis (see Fig. 14). The latter one is determined via Eq. (B30) and the measured intensities of the two CH_2-scissoring peaks. For confined $C_{16}H_{33}OH$, we have $I_a=13.29$ and $I_b=22.23$ yielding an angle of $\zeta=37.7°$ [see Fig. 12(b) for $T=245$ K]. We display the intermolecular force constants in Table IV. For comparison, we also list literature values for an alkane, $C_{23}H_{48}$ at 90 K, which have been evaluated in the same way.[40] This alkane and $C_{16}H_{33}OH$ exhibit a similar structure. The backbones of the molecules consist of the same CH_2 units and both take the β form at low temperatures. In addition, also the values of the lattice constants for $C_{23}H_{48}$, $a=7.45$ Å, and $b=4.96$ Å are close to those of $C_{16}H_{33}OH$ (see Table I). Due to this structural similarity, the intermolecular distances listed in Table IV are similar, however, the respective force constants differ slightly by 10%–20%. This is mainly due to the orientation of CH_2 groups (the projection of the backbones on the *a*-*b* plane) characterized by the herringbone angle ζ. For $C_{16}H_{33}OH$, $\zeta=37.7°$ holds; for the alkane $\zeta=42°$.

TABLE IV. Distances between two neighboring hydrogen atoms and the resulting interaction force constants in the C phase confined $C_{16}H_{33}OH$ (β form). ζ denotes the herringbone angle between the projection of the backbone and the *a* axis (see Fig. 14). For comparison, we also list literature values for an alkane, $C_{23}H_{48}$ at 90 K, that also takes the β form (Ref. 40). The CH_2 backbones of both molecules are similar, but $C_{16}H_{33}OH$ exhibits an additional polar OH group that affects the orientation angle ζ.

		Confined $C_{16}H_{33}OH$ (this work) $\zeta=37.7°$		Bulk $C_{23}H_{48}$ [a] $\zeta=42°$	
H atoms	Force constant	distances (Å)	10^{-21} Nm	distances (Å)	10^{-21} Nm
3–2′	$f_{3,2'}$	2.85	−4.674	2.79	−5.837
3–5	$f_{3,5}$	2.59	−2.775	2.70	−2.376
3–6	$f_{3,6}$	2.96	−3.508	2.94	−3.920
3–6′	$f_{3,6'}$	2.96	−3.508	2.94	−3.920

[a]Reference 40.

This difference is probably due to the presence of polar OH groups in $C_{16}H_{33}OH$ that are strongly interacting and thus have an impact on the molecular orientation. The above comparison confirms once again that confined $C_{16}H_{33}OH$ takes the β form in contrast to the bulk material (γ and β forms).

In order to assess the validity of our analysis, we also calculate the theoretical band splitting of the CH_2-scissoring vibration and compare it with the measured values. Using the values from Table IV as well as Eqs. (B34) and (B35), we get a theoretical value of $\Delta\bar{\nu}_{calc}=8.1$ cm^{-1} for confined $C_{16}H_{33}OH$ at $T=245$ K. The measured band splitting is $\Delta\bar{\nu}_{meas}=7.8$ cm^{-1}. Therefore, the experimental data are in good agreement with the theory.

IV. SUMMARY

We have studied the structure and molecular dynamics of *n*-hexadecanol confined in nanochannels of mesoporous silicon and of bulk *n*-hexadecanol in their respective phases (in the order of decreasing temperature: liquid, rotator R_{II}, and C). For this purpose, we have performed x-ray and infrared measurements.

The transition temperatures for confined $C_{16}H_{33}OH$ are lower than for bulk $C_{16}H_{33}OH$ ($\Delta T\simeq 20$ K; see Table II). In addition, under confinement, the phase transitions are smeared, probably due to a distribution of pore diameters. Geometrical confinement does not affect the innermolecular force constants of the CH_2-scissoring vibration (see Table III) but has an impact on the molecular arrangement. The R_{II} phase of both bulk and confined hexadecanol is characterized by an orthorhombic subcell, where the chain axis is parallel to the layer normal (see Fig. 4). However, in the low-temperature C phase, there is a fundamental structural difference. While bulk $C_{16}H_{33}OH$ exhibits a polycrystalline mixture of β and γ forms (see Figs. 2 and 3), geometrical confinement favors a phase closely related to the β form. Only crystallites with an orthorhombic subcell are formed, where the chain axes are parallel to the bilayer normal. However, the γ form having a monoclinic subcell, in which the chain axis is tilted with respect to the layer normal, is suppressed. A reason for this might be the irregular shape of the nanochannels, into which the crystallites have to fit, favoring the formation of the geometrically more simple and less bulky form[3,39] (see Fig. 6). Since only the pure β form is present under confinement, we were able to evaluate the intermolecular force constants of the CH_2-scissor vibration. Also the orientation of the β crystallites has been deter-

mined. The molecules are arranged with their long axis perpendicular to the pore axis.

APPENDIX A

In this section, we show how the innermolecular force constants of the CH_2 groups can be evaluated using three characteristic vibration frequencies that are easily measured: the scissor vibration as well as the symmetric and asymmetric CH-bond stretching. For this purpose, we apply the Wilson FG-matrix method.[42] We use the notation of Meister and Cleveland[41] for the similar H_2O molecule and perform the calculations in the same way.

Figure 13 shows a single CH_2 molecule. In the following, we will neglect the influence of the neighboring molecules on this one. $d=1.09$ Å is the length of the C-H bond and $\alpha=109.47°$ is the angle between the two C-H bonds.[32] This kind of molecule belongs to the C_{2_ν} point group. This means, there are two vibrations of type A_1 (symmetric stretching and bending vibration) and one vibration of type B_2 (asymmetric stretching vibration). The internal coordinates of this molecule are Δd_1, Δd_2, and $\Delta\alpha$. Δd_1 and Δd_2 mean changes in the bond length of the two C-H bonds and $\Delta\alpha$ changes in the angle between the two bonds. Therefore, we get three symmetry coordinates: two for A_1 and one for B_2. If we assume d being the equilibrium C-H bond length, then we obtain for the three symmetry coordinates,

$$R_1 = \sqrt{\frac{1}{2}}\Delta d_1 + \sqrt{\frac{1}{2}}\Delta d_2, \tag{A1}$$

$$R_2 = \Delta\alpha \cdot d, \tag{A2}$$

$$R_3 = \sqrt{\frac{1}{2}}\Delta d_1 - \sqrt{\frac{1}{2}}\Delta d_2. \tag{A3}$$

Now, we have to calculate the **F** matrix related to the potential energy and the **G** matrix related to the kinetic energy. The potential energy can be written as

$$2V = \sum f_{ik} r_i r_k \tag{A4}$$

and with the internal coordinates

$$2V = f_d[(\Delta d_1)^2 + (\Delta d_2)^2] + f_\alpha (d\Delta\alpha)^2 + 2f_{d\alpha}(\Delta d_1 + \Delta d_2) \times (d\Delta\alpha) + 2f_{dd}(\Delta d_1)(\Delta d_2). \tag{A5}$$

Now we set $d_1=d_2=d$ and write Eq. (A5) as

$$2V = \sum F_{jl} R_j R_l, \tag{A6}$$

with $F_{jl}=F_{lj}$. In matrix form, Eqs. (A4) and (A5) become

$$2V = \mathbf{r}'\mathbf{f}\mathbf{r} \tag{A7}$$

and

$$2V = \mathbf{R}'\mathbf{F}\mathbf{R} \tag{A8}$$

$\mathbf{r}'$ and $\mathbf{R}'$ are the transposes of $\mathbf{r}$ and $\mathbf{R}$. With Eqs. (A7) and (A8)

$$\mathbf{r}'\mathbf{f}\mathbf{r} = \mathbf{R}'\mathbf{F}\mathbf{R}. \tag{A9}$$

The R_i's are linear combinations of the r_i's

$$R_i = \sum_k U_{ik} r_k,$$

$$\mathbf{R} = \mathbf{U}\mathbf{r}. \tag{A10}$$

Since the R_i's are orthogonal and normalized then $\mathbf{U}^{-1}=\mathbf{U}'$ and

$$\mathbf{r} = \mathbf{U}'\mathbf{R}, \tag{A11}$$

$$\mathbf{r}' = (\mathbf{U}'\mathbf{R}) = \mathbf{R}'\mathbf{U}. \tag{A12}$$

This means with Eq. (A10)

$$\mathbf{R}'(\mathbf{U}\mathbf{f}\mathbf{U}')\mathbf{R} = \mathbf{R}'\mathbf{F}\mathbf{R}, \tag{A13}$$

$$\mathbf{F} = \mathbf{U}\mathbf{f}\mathbf{U}'. \tag{A14}$$

The **F** matrix is

	Δd_1	Δd_2	$\Delta\alpha$
Δd_1	f_d	f_{dd}	$df_{d\alpha}$
Δd_2	f_{dd}	f_d	$df_{d\alpha}$
$\Delta\alpha$	$df_{d\alpha}$	$df_{d\alpha}$	$d^2 f_\alpha$

The **U** matrix for type A_1 is

A_1	Δd_1	Δd_2	$\Delta\alpha$
R_1	$\sqrt{\frac{1}{2}}$	$\sqrt{\frac{1}{2}}$	0
R_2	0	0	1

and for B_2

B_2	Δd_1	Δd_2	$\Delta\alpha$
R_3	$\sqrt{\frac{1}{2}}$	$-\sqrt{\frac{1}{2}}$	0

So, for the type A_1 the **F** matrix is

$$\mathbf{F}_{A_1} = \mathbf{U}\mathbf{f}\mathbf{U}' = \begin{pmatrix} F_{11} & F_{12} \\ F_{21} & F_{22} \end{pmatrix} = \begin{pmatrix} f_d + f_{dd} & \sqrt{2} df_\alpha \\ \sqrt{2} df_\alpha & d^2 f_\alpha \end{pmatrix}, \tag{A15}$$

and for the B_2 type

$$\mathbf{F}_{B_2} = (F_{33}) = (f_d - f_{dd}). \tag{A16}$$

The exact derivation of the **G** matrix should not be shown here. It can be gleaned by Meister and Cleveland.[41] Only the most important steps shall be explained here.

If only nondegenerate vibrations are present, the elements of the kinetic-energy matrix can be written as

$$G_{jl} = \sum_p \mu_p g_p \mathbf{S}_j^{(t)} \mathbf{S}_l^{(t)}, \tag{A17}$$

where j and l refer to symmetry coordinates used in determining the **S** vector; p refers to a set of equivalent atoms, a typical one of the set being t. μ_p is the reciprocal of the mass

of the typical atom t_p and g_p is the number of equivalent atoms in the pth set. The **S** vector is given by

$$\mathbf{S}_j^{(t)} = \sum_k U_{jk} s_{kt}, \tag{A18}$$

where j, U_{jk}, and Σ_k have the same meaning as above. s_{kt} can be expressed in terms of unit vectors along the chemical bonds and depends on the changes in the bond length or the angle between the bonds. So, the **G** matrix for the A_1 vibration type has the form

$$\mathbf{G}_{A_1} = \begin{pmatrix} G_{11} & G_{12} \\ G_{21} & G_{22} \end{pmatrix} = \begin{pmatrix} \mu_H + \mu_C(1+\cos\alpha) & -\dfrac{\mu_C\sqrt{(2)}\sin\alpha}{d} \\ -\dfrac{\mu_C\sqrt{(2)}\sin\alpha}{d} & \dfrac{2\mu_H + \mu_C(1-\cos\alpha)}{d} \end{pmatrix} \tag{A19}$$

and for the B_2 vibration type,

$$\mathbf{G}_{B_2}(G_{33}) = [\mu_H + \mu_C(1-\cos\alpha)]. \tag{A20}$$

To determine the frequencies, one has to solve the equation

$$|\mathbf{GF} - \lambda\mathbf{E}| = 0, \tag{A21}$$

where $\lambda = \omega^2 = (\bar{\nu} 2\pi c)^2$ denotes the square of the angular frequency. For the A_1 type, one gets the equation

$$\lambda^2 - \lambda(F_{11}G_{11} + 2F_{12}G_{12} + F_{22}G_{22}) + \begin{vmatrix} F_{11} & F_{12} \\ F_{21} & F_{22} \end{vmatrix} \cdot \begin{vmatrix} G_{11} & G_{12} \\ G_{21} & G_{22} \end{vmatrix} = 0 \tag{A22}$$

and for the B_2 type

$$\lambda_3 - F_{33}G_{33} = 0. \tag{A23}$$

Equation (A22) can be separated with the Vieta expression.[43] Inserting the terms for the F_{ij} and G_{ij}, we obtain

$$\lambda_1 + \lambda_2 = (f_d + f_{dd})[\mu_C(1+\cos\alpha) + \mu_H] + 2f_\alpha[\mu_C(1-\cos\alpha) + \mu_H] - 4f_{d\alpha}\mu_C \sin\alpha,$$

$$\lambda_1 \cdot \lambda_2 = [(f_d + f_{dd})f_\alpha - 2f_{d\alpha}^2]2\mu_H(2\mu_C + \mu_H). \tag{A24}$$

For Eq. (A23) one obtains

$$\lambda_3 = (f_d - f_{dd})[\mu_C(1-\cos\alpha) + \mu_H]. \tag{A25}$$

Neglecting the coupling constants f_{dd} and $f_{d\alpha}$ allows to evaluate the innermolecular force constants using the measured wave numbers, $\bar{\nu}_{d,\mathrm{sym}} = \sqrt{\lambda_1}/(2\pi c)$, $\bar{\nu}_\alpha = \sqrt{\lambda_2}/(2\pi c)$, and $\bar{\nu}_{d,\mathrm{asym}} = \sqrt{\lambda_3}/(2\pi c)$. Then Eq. (A25) yields

$$f_d = (2\pi c)^2 \frac{\bar{\nu}_{d,\mathrm{asym}}^2}{\mu_C(1-\cos\alpha) + \mu_H}. \tag{A26}$$

Inserting this result into Eq. (A24) yields

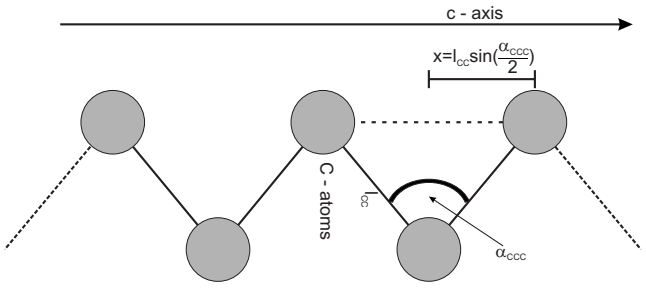

FIG. 15. Lateral view at the long axis of the $C_{16}H_{33}OH$ chain; x is the projection of the C-C distance on the c axis of the crystal lattice.

$$f_\alpha = (2\pi c)^2 \frac{\bar{\nu}_{d,\mathrm{sym}}^2 \cdot \bar{\nu}_\alpha^2}{\bar{\nu}_{d,\mathrm{asym}}^2} \frac{\mu_C(1-\cos\alpha) + \mu_H}{2\mu_H(2\mu_C + \mu_H)}. \tag{A27}$$

There is a second possibility to evaluate f_α, i.e., by inserting Eq. (A26) into Eq. (A24). This yields

$$f_\alpha = (2\pi c)^2 \frac{\bar{\nu}_{d,\mathrm{sym}}^2 + \bar{\nu}_\alpha^2 - \bar{\nu}_{d,\mathrm{asym}}^2 \frac{\mu_C(1+\cos\alpha)+\mu_H}{\mu_C(1-\cos\alpha)+\mu_H}}{2[\mu_C(1-\cos\alpha) + \mu_H]}. \tag{A28}$$

Taking the measured wave numbers listed in Table III and the average angle between the CH bonds, $\alpha = 109.4°$, as well as the masses of the atoms, $1/\mu_C = 12u$, and $1/\mu_H = 1u$ ($u = 1.660\,6 \times 10^{-27}$ kg), Eqs. (A26)–(A28) yield the force constants listed in Table III. The difference in calculating f_α via Eq. (A27) or Eq. (A28) is below 3.1% confirming that the innermolecular coupling terms can be neglected.

APPENDIX B

What follows is a summary of Snyder's[40] derivation of the intermolecular force constants between the CH_2 groups of neighboring molecules that gives rise to a splitting of the scissor band at low temperatures. We show how this formalism can be applied to $C_{16}H_{33}OH$. An alternative description can be found in Ref. 44.

In Fig. 14 we display a hexagonal subcell of $C_{16}H_{33}OH$. While Stein[45] took only one pair of neighboring CH_2 into account to calculate the splitting of rocking and scissoring bands, Snyder has shown that more pairs had to be included. When we consider the distances of H atoms from the H atom no. 3 (see Fig. 14) then all atoms except no. 2′, 6′, 5, and 6 have distances larger then 3.7 Å. The internal coordinates α_i are always half of the angle between the C-H bonds of a CH_2 molecule. Solid circles are H atoms in the same plane; dashed circles are H atoms in a plane above or below.

Now, we want to write the positions of these five H atoms as vectors. Figure 15 shows the lateral view of a part of the $C_{16}H_{33}OH$ chain. With values from Abrahamsson *et al.*[32] for $l_{CC} = 1.545$ Å and $\alpha_{CCC} = 110.4°$, we can calculate the distance of the a-b plane to the corresponding plane above or below with,

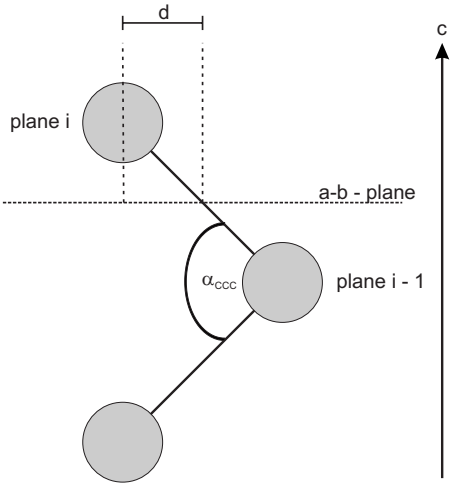

FIG. 16. Lateral view at the long axis of the $C_{16}H_{33}OH$ chain; d is the projection of half of the C-C distance on the a-b plane of the subcell.

$$x = l_{CC} \sin\left(\frac{\alpha_{CCC}}{2}\right) = 1.268\ 7\ \text{Å}.$$

Assuming that the hydrogen in the central plane has the c component 0, the hydrogen in the plane above has the component $c = 1.268\ 7$ Å.

The projection of the C-C bond in the a-b plane is according to Fig. 16,

$$d = \frac{l_{CC}}{2}\cos\left(\frac{\alpha_{CCC}}{2}\right) = 0.440\ 9\ \text{Å}.$$

Taking the point **0** for the lower left edge of the ab plane, the five atoms have the coordinates:

$$H_3 = \begin{pmatrix} \frac{a}{2} - d\cos(\zeta) - l\cos(\alpha_3 - \zeta) \\ \frac{b}{2} + d\sin(\zeta) - l\sin(\alpha_3 - \zeta) \\ 0 \end{pmatrix},$$

$$H_{2'} = \begin{pmatrix} -d\cos(\zeta) + l\sin\left(\alpha_{2'} - \frac{\pi}{2} + \zeta\right) \\ b - d\sin(\zeta) - l\cos\left(\alpha_{2'} - \frac{\pi}{2} + \zeta\right) \\ 0 \end{pmatrix},$$

$$H_5 = \begin{pmatrix} d\cos(\zeta) - l\sin\left(\alpha_5 - \frac{\pi}{2} + \zeta\right) \\ d\sin(\zeta) + l\cos\left(\alpha_5 - \frac{\pi}{2} + \zeta\right) \\ 1.267\ 4 \end{pmatrix},$$

$$H_6 = \begin{pmatrix} d\cos(\zeta) + l\cos(\alpha_6 - \zeta) \\ d\sin(\zeta) - l\sin(\alpha_6 - \zeta) \\ 1.267\ 4 \end{pmatrix},$$

$$H_{6'} = \begin{pmatrix} d\cos(\zeta) + l\cos(\alpha_{6'} - \zeta) \\ b + d\sin(\zeta) - l\cos(\alpha_{6'} - \zeta) \\ 1.267\ 4 \end{pmatrix},$$

with a and b being the lattice constants of the crystalline phase. We get the distances between the atom 3 and the other ones (see Fig. 14) with

$$r_{3j} = |H_3 - H_j|, \tag{B29}$$

where $j = 2', 6', 5, 6$ is. The herringbone angle ζ (see the upper left corner of Fig. 14) can be determined with the relation[40]

$$\frac{I_a}{I_b} = \tan^2\zeta, \tag{B30}$$

where I_a is the integrated intensity of the scissoring mode, which is polarized in the a direction (higher mode at 1473 cm^{-1}) and I_b the one of the mode, which is polarized in the b direction (lower mode at 1462 cm^{-1}).

With the distances of two hydrogen atoms H_3 and H_j($=r_{3,j}$) [in our case, 3 denotes the central H atom (see Fig. 14) and $j = 2'$, 5, 6, and $6'$ are the neighboring H atoms that interact], we obtain the intermolecular force constants $f_{3,j}$,

$$f_{3,j} = \frac{\partial^2 V_{HH}}{\partial\alpha_3\,\partial\,\alpha_j} = \left(\frac{\partial^2 V_{HH}}{\partial r^2}\right)_{r_{3j}} \left(\frac{\partial r}{\partial\alpha_3}\right)\left(\frac{\partial r}{\partial\alpha_j}\right), \tag{B31}$$

where V_{HH} is the hydrogen repulsion potential introduced by Dows,[46]

$$V_{HH} = 1.2 \times 10^{-10} e^{-3.52r}, \tag{B32}$$

with r in Å.

The values of $(\partial^2 V_{HH}/\partial r^2)_{r_{ij}}$ are obtained from Eq. (B33),

$$\beta = \frac{\partial^2 V_{HH}}{\partial r^2} = 1.486\ 848 \times 10^{-9} e^{-3.52r}, \tag{B33}$$

with β in $\frac{\text{ergs}}{\text{Å}^2} = 10^{16}\frac{\text{dyne}}{\text{cm}} = 10^{13}\frac{N}{m}$.

The measured intensity ratio [Eq. (B30)] allows us to calculate the distances r_{ij} as well as the partial derivatives $\partial r/\partial\alpha_i$ [see Eq. (A28) and above]. Finally, by knowing the intermolecular force constants $f_{3,j}$ from Eq. (B33), we can evaluate the band splitting of the scissoring vibration.[40] For the angular frequencies,

$$\bar{\nu}_1^2 - \bar{\nu}_2^2 = \left(\frac{1}{2\pi c}\right)^2 \underbrace{G_a^B \cdot \{2f_{3,2'} - 2(f_{3,6} + f_{3,6'}) - 4f_{3,5}\}}_{\Delta\lambda^B} \tag{B34}$$

holds [in Snyder's general theory, the force constants

for the scissoring vibration are denominated as $f_a^3(=f_{3,2'})$, $f_b^2(=f_{3,6}+f_{3,6'})$, and $f_b^3(=f_{3,5})$] with

$$G_a^B = \tfrac{4}{3}Q_R^2\mu_C + Q_r^2\mu_H. \tag{B35}$$

Here $1/\mu_C = 12u$ and $1/\mu_H = 1u$ denote the masses of the atoms ($u = 1.660\,6 \times 10^{-27}$ kg), $1/Q_R = 1.545 \times 10^{-10}$ m the C-C distance, and $1/Q_r = 1.09 \times 10^{-10}$ m the C-H distance, so that $G_a^B = (0.888\,25/u)$ Å$^{-2} = 5.349 \times 10^{46}$ (N m)$^{-1}$ s^{-2}. For the band splitting of the wave numbers, we thus obtain

$$\Delta\bar{\nu} = \bar{\nu}_1 - \bar{\nu}_2 = \left(\frac{1}{2\pi c}\right)^2 G_a^B \cdot \frac{\{2f_{3,2'} - 2(f_{3,6} + f_{3,6'}) - 4f_{3,5}\}}{\bar{\nu}_1 + \bar{\nu}_2}. \tag{B36}$$

Inserting the values of Table IV, i.e., $[2f_{3,2'} - 2(f_{3,6} + f_{3,6'}) - 4f_{3,5}] = 15.784 \times 10^{-21}$ Nm for confined $C_{16}H_{33}OH$, as well as the respective wave numbers that we take from Fig. 11 at low temperatures (labels 1a and 1b: $\bar{\nu}_1 + \bar{\nu}_2 \simeq 2 \cdot 146700\ 1/\mathrm{m}$), we get $\Delta\bar{\nu} = 810\ \mathrm{m}^{-1} \equiv 8.1\ \mathrm{cm}^{-1}$ for confined $C_{16}H_{33}OH$.[47]

[1] L. D. Gelb, K. E. Gubbins, R. Radhakrishnan, and M. Sliwinska-Bartkowiak, Rep. Prog. Phys. **62**, 1573 (1999).
[2] C. Alba-Simionesco, B. Coasne, G. Dosseh, G. Dudziak, K. E. Gubbins, R. Radhakrishnan, and M. G. Sliwinska-Bartkowiak, J. Phys.: Condens. Matter **18**, R15 (2006).
[3] H. K. Christenson, J. Phys.: Condens. Matter **13**, R95 (2001).
[4] K. Knorr, P. Huber, and D. Wallacher, Z. Phys. Chem. **222**, 257 (2008).
[5] J. Koppensteiner, W. Schranz, and M. R. Puica, Phys. Rev. B **78**, 054203 (2008).
[6] P. Scheidler, W. Kob, and K. Binder, Europhys. Lett. **52**, 277 (2000).
[7] F. Kremer, A. Huwe, M. Arndt, P. Behrens, and W. Schwieger, J. Phys.: Condens. Matter **11**, A175 (1999).
[8] C. L. Jackson and G. B. McKenna, J. Non-Cryst. Solids **131-133**, 221 (1991).
[9] G. Barut, P. Pissis, R. Pelster, and G. Nimtz, Phys. Rev. Lett. **80**, 3543 (1998).
[10] R. Pelster, Phys. Rev. B **59**, 9214 (1999).
[11] D. Daoukaki, G. Barut, R. Pelster, G. Nimtz, A. Kyritsis, and P. Pissis, Phys. Rev. B **58**, 5336 (1998).
[12] P. Pissis, A. Kyritsis, D. Daoukaki, G. Barut, R. Pelster, and G. Nimtz, J. Phys.: Condens. Matter **10**, 6205 (1998).
[13] W. Schranz, M. R. Puica, J. Koppensteiner, H. Kabelka, and A. V. Kityk, EPL **79**, 36003 (2007).
[14] B. Frick, M. Koza, and R. Zorn, Eur. Phys. J. E **12**, 3 (2003).
[15] K. Knorr, D. Wallacher, P. Huber, V. Soprunyuk, and R. Ackermann, Eur. Phys. J. E **12**, 51 (2003).
[16] D. Wallacher, R. Ackermann, P. Huber, M. Enderle, and K. Knorr, Phys. Rev. B **64**, 184203 (2001).
[17] P. Huber, D. Wallacher, and K. Knorr, J. Low Temp. Phys. **111**, 419 (1998); P. Huber and K. Knorr, Phys. Rev. B **60**, 12657 (1999); P. Huber, D. Wallacher, and K. Knorr, *ibid.* **60**, 12666 (1999).
[18] P. Huber, V. P. Soprunyuk, and K. Knorr, Phys. Rev. E **74**, 031610 (2006).
[19] A. Henschel, T. Hofmann, P. Huber, and K. Knorr, Phys. Rev. E **75**, 021607 (2007).
[20] R. Montenegro and K. Landfester, Langmuir **19**, 5996 (2003).
[21] B. Xie, G. Liu, S. Jiang, Y. Zhao, and D. Wang, J. Phys. Chem. B **112**, 13310 (2008).
[22] R. Valiullin and A. Khokhlov, Phys. Rev. E **73**, 051605 (2006).
[23] *Liquid Crystals in Complex Geometries*, edited by G. Crawford and S. Zumer (Taylor and Francis, London, 1996).
[24] A. V. Kityk, M. Wolff, K. Knorr, D. Morineau, R. Lefort, and P. Huber, Phys. Rev. Lett. **101**, 187801 (2008).
[25] P. Huber, D. Wallacher, J. Albers, and K. Knorr, Europhys. Lett. **65**, 351 (2004).
[26] V. Lehmann and U. Gösele, Appl. Phys. Lett. **58**, 856 (1991); V. Lehmann, R. Stengl, and A. Luigart, Mater. Sci. Eng., B **69-70**, 11 (2000).
[27] X. G. Zhang, J. Electrochem. Soc. **151**, C69 (2004).
[28] A. G. Cullis, L. T. Canham, and P. D. J. Calcott, J. Appl. Phys. **82**, 909 (1997).
[29] S. Gruener and P. Huber, Phys. Rev. Lett. **100**, 064502 (2008).
[30] P. Huber, S. Gruener, C. Schaefer, K. Knorr, and A. V. Kityk, Eur. J. Phys. **141**, 101 (2007).
[31] V. Métivaud, A. Lefèvre, L. Ventolà, P. Négrier, E. Moreno, T. Calvet, D. Mondieig, and M. A. Cuevas-Diarte, Chem. Mater. **17**, 3302 (2005).
[32] S. Abrahamsson, G. Larsson, and E. von Sydow, Acta Crystallogr. **13**, 770 (1960).
[33] M. Tasumi, T. Shimanouchi, A. Watanabe, and R. Goto, Spectrochim. Acta **20**, 629 (1964).
[34] L. Ventolà, M. Ramirez, T. Calvet, X. Solans, M. A. Cuevas-Diarte, P. Negrier, D. Mondieig, J. C. van Miltenburg, and H. A. J. Oonk, Chem. Mater. **14**, 508 (2002).
[35] E. B. Sirota and X. Z. Wu, J. Chem. Phys. **105**, 7763 (1996).
[36] A. Henschel, P. Huber, and K. Knorr, Phys. Rev. E **77**, 042602 (2008).
[37] M. Steinhart, P. Göring, H. Dernaika, M. Prabhukaran, U. Gösele, E. Hempel, and T. Thurn-Albrecht, Phys. Rev. Lett. **97**, 027801 (2006).
[38] P. A. Palibin and A. I. Froiman, Z. Kristallogr. **85**, 322 (1933); P. W. Bridgman, Proc. Am. Acad. Arts Sci. **60**, 305 (1925).
[39] K. Morishige and K. Kawano, J. Chem. Phys. **112**, 11023 (2000).
[40] R. G. Snyder, J. Mol. Spectrosc. **7**, 116 (1961).
[41] A. G. Meister and F. F. Cleveland, Am. J. Phys. **14**, 13 (1946).
[42] E. B. Wilson, Jr., J. Chem. Phys. **7**, 1047 (1939).
[43] H. Siebert, *Anwendungen der Schwingungsspektroskopie in der anorganischen Chemie* (Springer-Verlag, Berlin, 1966).
[44] M. Tasumi and T. Shimanouchi, J. Chem. Phys. **43**, 1245 (1965).
[45] R. S. Stein, J. Chem. Phys. **23**, 734 (1955).
[46] D. A. Dows, J. Chem. Phys. **32**, 1342 (1960).
[47] J. deBoer, Physica **9**, 363 (1942).